

Additive Manufacturing of Self-Sensing Carbon Fiber Composites

Zhenpeng Xu, Haotian Lu, Qiyi Chen, Seokpum Kim, Vlastimil Kunc,
and Xiaoyu Rayne Zheng*

Carbon fiber-reinforced polymer (CFRP) composites have gained substantial attention across various industries owing to their exceptional mechanical properties and lightweight nature. The emergence of additive manufacturing technologies brings new opportunities to the industry, offering advantages such as design freedom, rapid prototyping, and customization. However, the fabrication of CFRP composites through 3D printing techniques poses challenges pertaining to low resolution and limitations in complex geometry realization. This work introduces digital light processing printing as a versatile, high-resolution method ideal for CFRP composite fabrication. The development and characterization of CFRP are focused on and the manipulation of mechanical properties through variations in matrix resins and fiber loadings is investigated, showcasing the versatility of CFRP composites for tailored applications. Additionally, the integration of self-sensing capabilities in CFRP structures is explored, which opens up opportunities for applications in smart components for automotive and structural health monitoring.

1. Introduction

Carbon fiber-reinforced polymer (CFRP) composites have attracted considerable interest across various industries

due to their extraordinary mechanical properties,^[1] lightweight nature,^[2] and corrosion resistance.^[3] These materials offer immense potential for applications in aerospace, automotive, construction, and many other sectors.^[4] Besides the mechanical performance enhancement, carbon fiber also introduces electrical conductivity, which enables the composites to be applied as a good candidate for self-sensing elements.^[4d,5] However, traditional manufacturing methods for CFRP composites involve a labor-intensive and time-consuming manual layup process for fiber/resin impregnation, leading to high production costs and slow manufacturing cycles.^[6] Besides, the fabrication process is intrinsically difficult in achieving complex geometries, limiting the design flexibility and customization.^[7] This undermines the performance of the CFRP composites and lacks the ability to create unique components to meet specific requirements.^[8]

The advent of additive manufacturing (AM) technologies has expanded the fabrication of CFRP composites owing to its unparalleled freedom in geometry design and fabrication. For example, fused deposition modeling (FDM) allows for the fabrication of complex-shaped CFRP composites by extruding a carbon fiber-incorporated thermoplastic filament. However, FDM encounters difficulties in attaining desirable mechanical properties owing to inadequate layer adhesion and constrained material diversity within the thermoplastic domain. Direct ink writing (DIW) has been widely applied in the 3D printing of CFRP, which allows the use of mechanically robust thermoset material and eliminates the layer delamination problem. However, the unsatisfying printing resolution and difficulty in large-scale production hinder the applications of DIW printed CFRP. Compared to these AM methods, digital light processing (DLP) printing, which uses photopolymerization to build intricate 3D structures layer by layer, features better resolution and allows for the printing of functional composites.^[9] Consequently, it holds great promise for fabricating CFRP composites with robust mechanical properties along with sensing capabilities.^[10] However, DLP-printed CFRP and its sensing capability have not been studied, primarily due to the difficulties associated with handling the viscous resin and the need to optimize the printing process.

In this study, we exploited DLP 3D printing approach and optimized the processability of CFRP resin under UV exposure, to

Z. Xu, H. Lu, Q. Chen, X. R. Zheng
Department of Material Science and Engineering
University of California Berkeley
Berkeley, CA 94720, USA
E-mail: rayne23@berkeley.edu

Z. Xu, X. R. Zheng
Department of Civil and Environmental Engineering
University of California Los Angeles
Los Angeles, CA 90095, USA

H. Lu, X. R. Zheng
Department of Mechanical and Aerospace Engineering
University of California Los Angeles
Los Angeles, CA 90095, USA

S. Kim, V. Kunc
Manufacturing Science Division
Oak Ridge National Laboratory
Oak Ridge, TN 37831, USA

X. R. Zheng
California NanoSystems Institute
University of California Los Angeles
Los Angeles, CA 90095, USA

 The ORCID identification number(s) for the author(s) of this article can be found under <https://doi.org/10.1002/adem.202301249>.

DOI: 10.1002/adem.202301249

fabricate the CFRP composites with excellent printing quality, tailororable mechanical properties, and self-sensing capabilities. The incorporated carbon fiber significantly enhanced the mechanical strength and worked as an electrically conductive agent offering excellent self-sensing behavior. The mechanical properties and self-sensing performance have been investigated by varying matrix resin compositions, fiber loadings, and fiber lengths. We fabricated materials with a wide range of mechanical properties, maximizing the stiffness-damping pair through two-phase structures, and explored their tunability through various material combinations. We achieved an excellent self-sensing behavior using carbon fiber with a length of 315 μm . We printed 3D architected CFRP composites and demonstrated that these microarchitectures can monitor and respond to external stimuli, such as pressure and strain, thereby presenting new opportunities for intelligent and self-sensing structural components in automotive and structural health monitoring applications.

2. Results and Discussions

2.1. System Setup and Fabrication Procedures

We introduced a methodology for printing CFRP composites using a state-of-the-art DLP printing system, building upon the authors' previous work.^[2,10a] As depicted in Figure 1a, the setup comprised a high-resolution projection system and a custom-designed resin vat. The resin vat contained a resin formulation loaded with carbon fibers. The printing process involved the projection of digital light patterns (405 nm UV light) from beneath onto the resin vat, selectively curing resin layer by layer to form intricate structures. Two types of carbon fibers are incorporated into the resin: type A fiber has an average length of 70 μm and type B fiber has a length of 315 μm (see Experimental Section and Figure S1, Supporting Information). The resin recoating process is completed by lifting the build plate, allowing

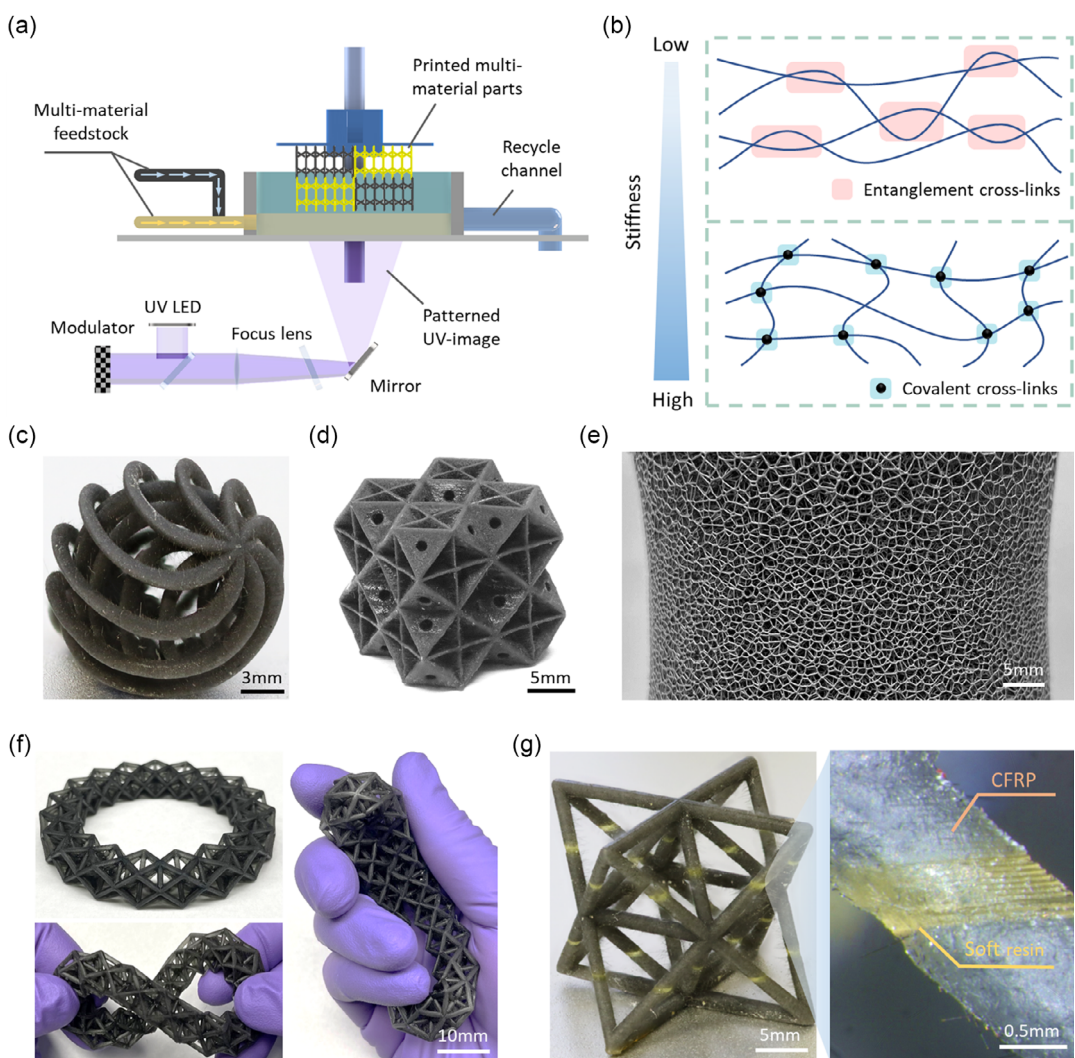


Figure 1. Setup of the DLP printing system and fabricated samples with variable stiffness. a) The DLP 3D printing system features a customized vat. b) Schematic illustrations showcasing the composition of the stiffness/soft resin without carbon fibers. c–e) Complex architectures fabricated using CFRP with a stiff matrix. f) Truss-lattice structure fabricated using CFRP with a soft matrix. g) Multimaterial octet-truss structure fabricated all at once using stiff CFRP and a soft resin.

the resin to settle for the subsequent layer. The addition of carbon fibers to the resin is observed to increase its viscosity, with longer fibers causing a more pronounced increase.

In our study, we focused on optimizing process parameters to achieve high-resolution CFRP printing with increased fiber loading. The presence of carbon fibers (types A and B) in the resin matrix benefits the mechanical properties, but it also affects the curing depth due to UV light impedance and increases the resin's viscosity, both of which can pose challenges to printability. Regarding the cure depth, it is observed that higher fiber loading and shorter fiber length result in more reduced cure depth, leading to potential delamination issues (see details in Figure S2, Supporting Information). To address this, we found that adding additional 1 wt% of photoinitiators to the matrix doubles the cure depth from 40 to 80 μm , facilitating the printing process.^[11] Another major challenge when using resins loaded with longer fibers is the increased viscosity caused by greater fiber entanglement and higher frictional resistance within the resin matrix. For instance, resin loaded with 5 wt% type B fibers exhibits a non-flowable state when a shear force is absent, posing challenges for actual printing. To enable printing with such viscous resin,

we applied a tape-casting method, effectively recoating the resin into a thin and uniform layer.^[2] This ensured the printing resolution was as small as the microscale level.

We have added carbon fibers to both stiff and soft matrix resins to demonstrate the printability of various CFRP composites. Figure 1c–e shows the printing of CFRP lattices made from stiff matrix resin, with the smallest feature size of less than 200 μm . Figure 1f demonstrates the printing of a flexible CFRP lattice ring based on an elastic matrix resin. Moreover, our custom DLP 3D printing system enables multimaterial printing that combines materials with distinct mechanical properties. As shown in Figure 1g, a stiff CFRP resin (black) and an elastomer (yellow) were printed together in an octet-truss structure, allowing for the simultaneous achievement of mutually exclusive properties.^[1,2]

2.2. Tailoring Stiffness-Damping Properties of CFRP Composites

The mechanical properties of CFRP composites can be easily tuned by using different resin matrices and fiber loadings, as

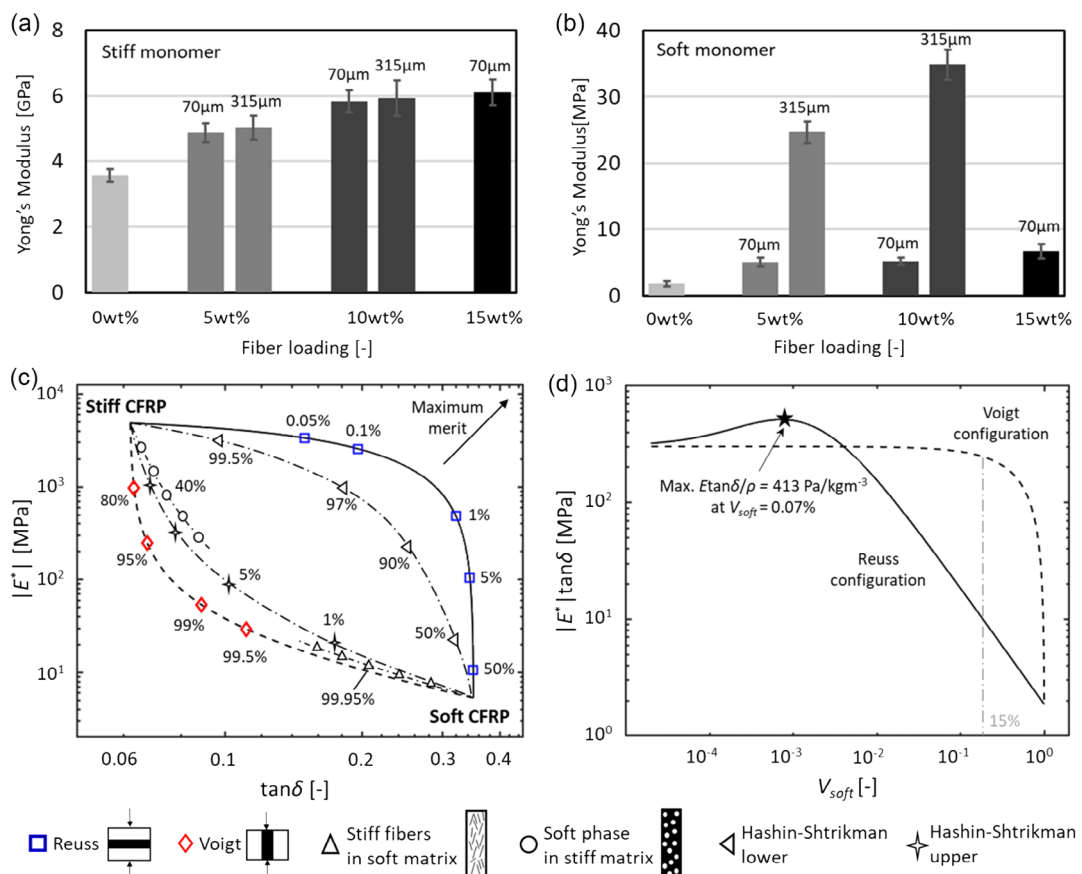


Figure 2. a) Young's modulus of CFRP with variable fiber concentrations and fiber types based on a stiff resin matrix (Formlabs Rigid 10K). b) Young's modulus of CFRP with variable fiber concentrations and fiber types based on a soft resin matrix (Formlabs Elastic 50A). c) Complex modulus versus loss tangent for various two-phase configurations incorporating stiff CFRP and soft CFRP of bulk material. The percentage corresponds to the volume fraction of soft CFRP. Graphical legends are provided at the bottom of this figure. d) Plot of $|E^*|\tan\delta$ with the volume fraction of soft CFRP, illustrating both Voigt and Reuss configurations.

illustrated in **Figure 2a,b**. Furthermore, we present a novel approach that can potentially create a new material with high stiffness-loss efficiency by strategically distributing and arranging the two types of CFRP composites (stiff and soft).

Based on measured mechanical properties, we first conducted an analytical study on several representative two-phase layouts by varying the volume fraction of the soft CFRP and computing their complex modulus ($|E^*|$) and loss tangent ($\tan\delta$) based on the two-phase composite theory.^[12] **Figure 2c** illustrates an $|E^*|$ – $\tan\delta$ relationship of different layouts, with the percentage corresponding to the volume fraction of soft CFRP. The layouts included Reuss (assumes that all components of a composite experience the same strain) and Voigt composites (assumes that all components of a composite material are subjected to the same stress), Hashin–Shtrickman composites, stiff fibers in a soft matrix, and soft phase in a stiff matrix. In these layouts, both stiff CFRP and soft CFRP had 5 wt% fiber loading (type A), and each composite was treated as a single phase. The percentage numbers in **Figure 2c** represent the volume fraction of soft CFRP within the composite. Calculations demonstrated that a small volume fraction of soft CFRP in the Reuss layout resulted in a substantial increase in loss tangent with a reasonable reduction in complex modulus. Conversely, the Voigt composite required a significant addition of the soft phase to achieve a noticeable increase in loss tangent. The upper and lower bounds of the Hashin–Shtrickman composites were bounded by those of the Voigt and Reuss composites, while the inclusion of stiff fibers and soft phase exhibited behavior similar to the Voigt composite.

The product of complex modulus and loss factor, $|E^*|\tan\delta$, can be used to exhibit compatibility of stiffness and damping in materials: a larger value indicates better performance. Therefore, the layouts were assessed to identify the maximum performance of $|E^*|\tan\delta$.^[13] **Figure 2d** demonstrates that the Reuss layout, with a volume fraction of soft CFRP approximately equal to 0.07%, exhibited the highest figure of merit. In contrast, the figure of merit for the Voigt configuration rapidly declined when the soft phase exceeded 15%.

The above-computed layouts can be realized through multimaterial printing or by mixing two composites to form a single-phase composite. For example, we mixed two CFRP composites (5 wt% type A) at ratios ranging from 0:100 to 100:0 (soft:stiff). These composites were anticipated to exhibit properties akin to the structural layout of soft phase embedded in a stiff matrix, improving the overall figure of merit. This is feasible as these composites can withstand mechanical stress without failure at low strains, thus boosting their energy absorption. The behavior and characteristics supporting this claim can be observed in **Figure S3**, Supporting Information. It is worth highlighting that our approach is capable of producing a variety of materials that span a wide spectrum in terms of mechanical properties.

2.3. Investigation of Electrical Properties of CFRP Composites

Beyond the improved mechanical attributes, carbon fiber also introduces electrical conductivity, which endows the CFRP with self-sensing capability. This section aims to demonstrate the self-sensing response of the CFRP material to compression and tension. We specifically highlight key factors, including

linearity, sensitivity, and repeatability. Additionally, we studied variations in resistivity between different resins and their influences on sensing behavior, ensuring consistent and reliable self-sensing performance.

To investigate the coupled electrical and mechanical properties of the 3D printed CFRP, we established a testing apparatus (refer to the experimental section) as shown in **Figure 3a**. We selected type B carbon fiber as the filler, given its exceptional conductivity even at low fiber concentrations. We printed a stiff CFRP bulk sample and subjected it to quasistatic compression while measuring its resistance using a multimeter. The linear stress–strain response of the stiff CFRP under compression (**Figure 3a**) is attributed to its brittle matrix, while the nonlinear behavior during tension (**Figure 3b**) stems from the soft CFRP's elastic matrix material. Taking into account the dimensional changes due to strain, we derived the resistivity from the resistance measurements. Our observations indicated that the resistivity of the CFRP material decreases with increased compression strain, attributed to enhanced electrical contacts between carbon fibers as they come closer upon compression. Within 2% strain, the material exhibits good linearity in resistivity change, with a calculated gauge factor ($k = \frac{\Delta R/R_0}{\Delta e}$) of about –6.7. Conversely, under tension strain of samples comprised of soft CFRP matrix, the resistivity increases linearly with strains below 3%, with a gauge factor of 3.5 (shown in **Figure 3b**). Beyond this, however, the resistivity rapidly escalates, reaching significantly higher values.

To examine the impact of fiber loading on sensitivity, we compared the resistivity changes between samples with 5 and 10 wt% fiber loading (type B), as illustrated in **Figure 3c**. The printed samples underwent multiple cyclic compressive strains, within the linear resistivity change range, up to 2%, and we recorded the corresponding real-time resistance. As can be seen, for both fiber loadings, consistent and stable results were observed across multiple cycles. Notably, the resin with 10 wt% carbon fiber displayed a higher sensitivity, due to its higher fiber loading.

2.4. Directional Sensing

We have also fabricated a lattice structure based on hexagonal honeycomb topology for directional sensing demonstration. This structure can potentially be integrated into automotive components, such as bumper energy absorbers, to effectively detect external forces. **Figure 4a** illustrates the fabricated honeycomb lattice using CFRP resin loaded with 5 wt% type B carbon fibers, with two pairs of conductive electrodes on two walls. The electrodes were connected to a multimeter, capturing resistance changes. To assess its performance, we conducted tests under three different loading directions: 1, 2, and 3.

Figure 4b illustrates the variation in resistance in response to dynamic mechanical stimuli across a range of strain magnitudes along 3-direction. Data from only one pair of electrodes are presented because both pairs underwent similar external stresses within the structural walls. From the plot, we observe that when subjected to a 7.5% compressive strain, the resistance change parameter $\Delta R/R_0$ reached a substantial magnitude of up to 0.11, indicating significant deformation of the structure. Even at a 2.5% strain, the resistance change remained visible on

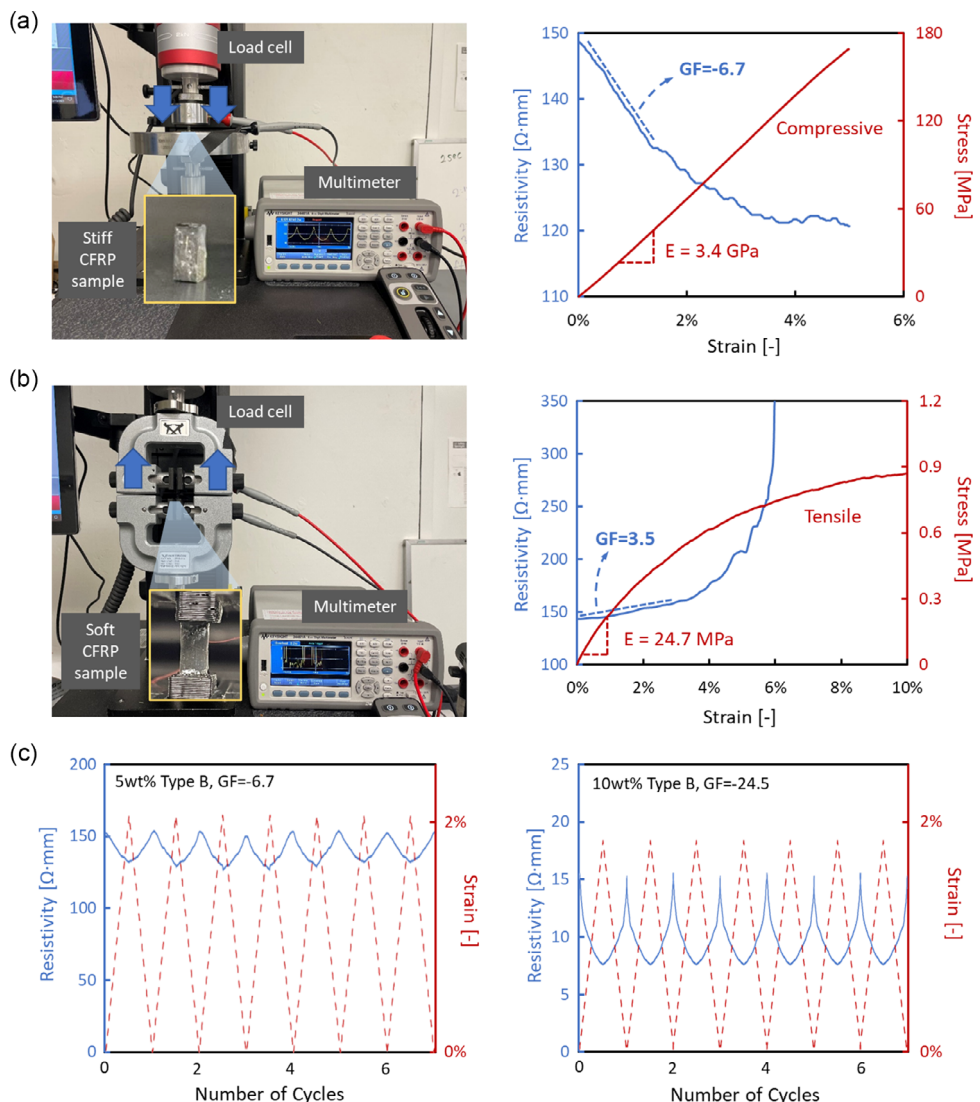


Figure 3. Coupled electrical and mechanical properties of printed CFRP samples showing self-sensing capability. a) Experimental setup for resistance measurement under in situ compressive loads, along with corresponding stress and resistivity measurements of a stiff CFRP sample loaded with 5 wt% type B fibers. b) Experimental setup for resistance measurement under in situ tensile loads, along with corresponding stress and resistivity measurements of a soft CFRP sample loaded with 5 wt% type B fibers. c) Measured resistivity under 2% quasistatic cyclic compressive strain of bulk CFRP materials with fiber concentrations of 5 and 10 wt%.

the plot. The small spike in resistance change is attributed to the micro-realignment of fibers and the uneven recovery rates inherent in the honeycomb lattice structure. The printed honeycomb building blocks also offer directional sensing capability. As shown in Figure 4c,d, ten cycles of compressive strains were applied along 1-direction and 2-direction, respectively. Figure 4c shows that the resistance change of electrode pair b was greater than that of electrode pair a. This difference can be attributed to the larger deformation of the unit cell wall in response to the external force. As a result, electrode pair a, situated on a less deformed, horizontally oriented wall, displayed a smaller resistance change. In contrast, when the impact was applied along 2-direction, the resistance change at electrode pair a surpassed that of pair b, as shown in Figure 4d. Apart from

differences in the wall deformation, the location shift of the fibers also played a significant role. When the external impact is applied along the axial direction for electrode pair a, the fibers within the wall undergo a relative shift, moving closer to each other due to the significant axial force transferred to the vertical wall. This proximity leads to more pronounced changes in resistivity (see simulation result in Supporting Information).

The directional sensitivity of the resistance change arises from the anisotropic nature of the honeycomb structure, where the deformation and load distribution vary depending on the direction of the applied force. To further enhance detection capabilities, it is possible to incorporate a greater number of electrodes within the honeycomb lattice structure. This can be achieved through the utilization of multimaterial printing and a selective

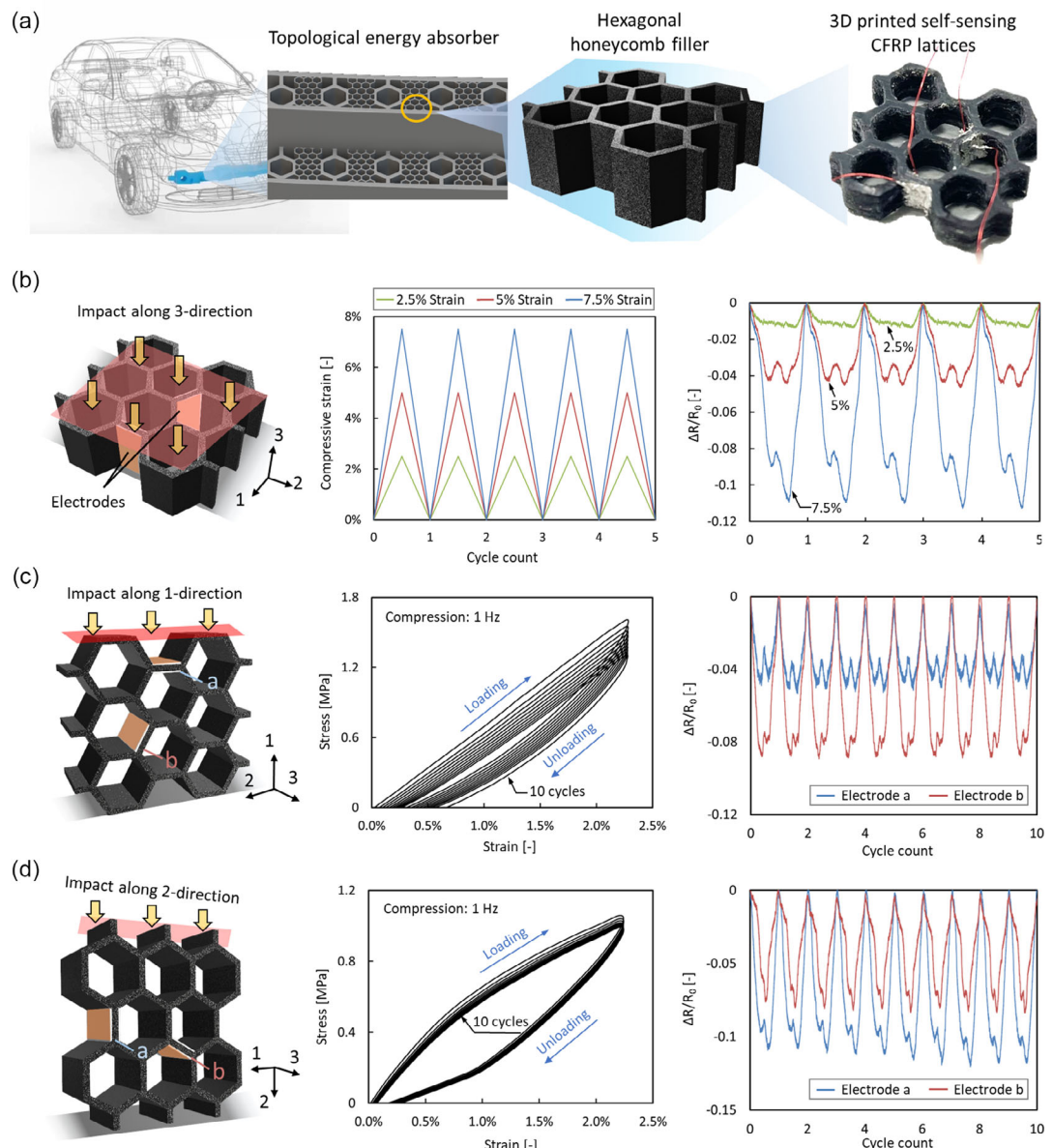


Figure 4. a) Printed honeycomb structure with self-sensing capability, suitable for automotive components. b) Measured change in resistivity upon impact with varying strain magnitudes along the 3-direction. c) Resistance change measurements of two electrodes when the impact is along the 1-direction, indicating a larger resistance change for electrode pair b. d) Conversely, resistance change measurements of two electrodes when the impact is along the 2-direction, revealing a larger resistance change for electrode pair a.

metal-plating process, which allows for the seamless integration of embedded electrodes within the honeycomb framework.^[9c] By strategically placing additional electrodes throughout the structure, a pressure mapping system can be realized, enabling improved sensitivity and accuracy in detecting variations and changes within the honeycomb lattice.

2.5. Mechanical Failure Mode Sensing

The application of CFRP composites could also be extended into the field of mechanical failure sensing, such as fractures and

buckling. The following elaboration further delineates an approach to understanding how mechanical failure mode is related to the resistivity changes in a lattice structure.

As shown in Figure 5a, to assess the overall structural integrity of the honeycomb lattice, we positioned a pair of electrodes on both sides of the honeycomb building block. This setup, designed to monitor fractures within the lattice, hinges on the inherent electrical conductivity of carbon fibers. The experiment involved compressing the lattice along 1-direction until it fractured. During this process, we noted three significant stress drops in the stress-strain plot at strains of approximately 4%,

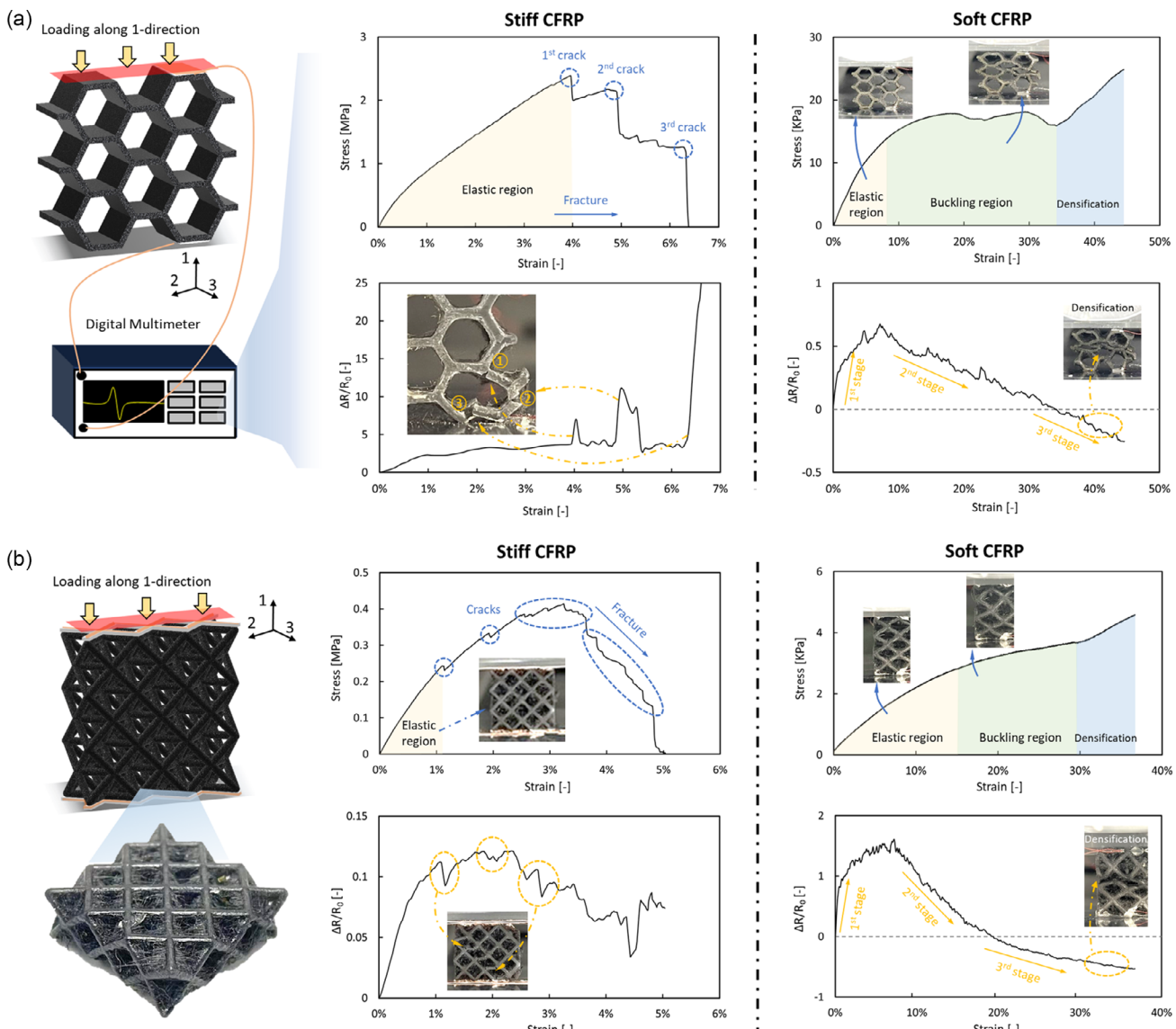


Figure 5. a) Mechanical and resistance response of stiff/soft honeycomb building block until fracture/densification. b) Mechanical and resistance response of stiff/soft octet lattice structure until fracture/densification.

5%, and 6.2%, which can be directly linked to the occurrence of cracks within the bottom unit cell of the stiff honeycomb lattice, as shown in the inset photo of Figure 5a. The resistance-change plot conversely mirrored this pattern with three major peaks aligning with the aforementioned strains. The peaks were notably higher when the cracks were larger, which is as expected because larger fractures yield more interruption of the conductive pathways within the lattice.

As for the same honeycomb structure made of soft CFRP, the stress–strain plot revealed three major regions corresponding to different stages of deformation: elastic, buckling, and densification. During the initial phase of deformation, the electrical resistance of the lattice increases with the strain until it started to decrease when the strain exceeded 8%. As the strain increased, buckling caused the cell walls to come closer, reducing resistance

by creating more conductive paths. When the strain exceeds about 34%, the lattice densifies. This irreversible deformation further decreases the resistance as the conductive fibers become more closely packed.

Moving to the octet-truss lattice structure, we employed a similar setup and tested the lattice's response to compression as shown in Figure 5b. The minor drops observed in the stress–strain curves indicated the fracture of the strut inside the stiff lattice, and the resistance-change plot mirrored these drops. As for the soft octet-truss lattice, its behavior closely resembled that of the soft honeycomb, both exhibiting buckling and densification processes, and the resistance-change plot showed a similar trend. Through each stage of deformation, the changes in resistance can provide real-time insights into the structural health of the CFRP composite. These composites

allow intricate 3D designs with embedded sensing, offer material versatility, and combine both mechanical strength and sensing within a broader print scale and superior resolution compared to many deposition-centric methods.^[14]

3. Conclusion

In conclusion, this work has made contributions to the development and characterization of self-sensing CFRP composites using the DLP printing process. By formulating CFRP resins with different matrix materials and fiber loadings, we have successfully achieved the manipulation of mechanical properties, opening up new avenues for tailored applications. The ability to precisely control the stiffness and other mechanical characteristics of CFRP composites holds great promise for industries such as construction, automotive, and aerospace. Furthermore, our study has demonstrated the self-sensing ability of CFRP composites through the integration of architectured lattices with localized electrodes. These structures enable time-resolved pressure sensing and structural health monitoring, paving the way for self-sensing smart materials under various loading conditions. Future research could delve into the optimization of DLP printed CFRP composites, specifically using locally aligned CFRPs to reinforce areas of structural vulnerability under load, such as nodes, multimaterial interfaces, or tension-bearing strut members within lattice structures.

4. Experimental Section

Materials and Resin Preparation: A group of UV curable CFRP composite made of UV-sensitive resin reinforced with short carbon fibers was prepared for printing. As the matrix material, a stiff and soft resin was purchased from Formlabs Inc. (Formlabs Rigid 10K, Formlabs Elastic 50A). The milled short carbon fibers were obtained from E&L Enterprises, Inc. (7 µm in diameter, ≈70/315 µm mean length, E&L Enterprises, Inc.). A photoinitiator, phenylbis(2,4,6-trimethylbenzoyl) phosphine oxide (Irg 819), and Sudan (I) were purchased from Sigma-Aldrich Inc. and used as an additional additive to the resin if needed. Batches start with 20 g of the matrix resin. Milled carbon fibers are added in 0, 1, 1.5, 2, and 3 g increments (0, 5, 7.5, 10, 15 wt%), followed by 24 h of mixing on a roller (Fisher Development, Inc.). Photoinitiator (0.2 g/0.4 g) and Sudan (0.0025 g) can be added before mixing if needed.

Fiber Length Distribution Measurement: To determine the fiber length distribution, a specific quantity of fibers was carefully placed onto a sheet of paper and spread evenly to facilitate their enumeration. Subsequently, an optical image capturing all the fibers was obtained using a microscope. The acquired images were then subjected to detailed analysis using ImageJ, an open-source software. Fiber length distribution maps were generated by employing various image processing techniques. Initially, an “Auto Local Threshold” plugin was utilized to highlight the fibers, effectively distinguishing them from the background. This step was followed by the application of a “Trainable Weka Segmentation” plugin, which successfully eliminated background noise and retained only the relevant fibers in the processed image. This enhanced the accuracy of subsequent measurements. The processed images, now containing the fibers of interest and minimal unwanted information, were used for measuring the fiber lengths. The measurements were performed using ImageJ’s measurement tools, taking into account the corrected scale size.

Cure Depth Measurement: A test pattern was projected onto a transparent FEP film, onto which resin had been applied. The light intensity of the projector was controlled by the pulse width modulation of the DMD chip throughout the operating refresh time. The UV exposure dose was

regulated by the predetermined exposure time and corresponding light intensity. Following exposure, any uncured suspension was removed by rinsing with ethanol. The cured layer was then bisected, and the thickness was measured using an optical camera (Dino-lite Inc.). The tested CFRP was based on Formlabs Rigid 10K.

Mechanical Testing: All tensile tests were conducted using the Instron 5944 universal testing machine (Instron Corporation, Norwood, MA). The printed dog bone specimens were elongated between the stationary and moving clamps. The applied loads were measured using the Instron load cell, which had a load capacity of 2000 N, while the displacements were measured using the integrated encoder linked to the crosshead movement. The stress-strain curves were subsequently computed based on the obtained data.

Piezoresistance Measurements under Compression: Before conducting the tests, a silver paste was applied to the side of the wall where the electrode was positioned. This step was taken to facilitate the connection of thin wires to the electrode and enable the measurement of electrical properties using a multimeter. The printed samples were cyclically compressed using the Instron machine with a predetermined maximum strain. The piezoresistance responses of the CFRP materials were measured in real time using a 34461A digital multimeter (KEYSIGHT, USA). The resistivity of the bulk CFRP material was subsequently calculated based on the geometric dimensions of the printed bulk CFRP. In the lattice test, the change in resistance, ΔR (calculated as the difference between the measured resistance R and the initial no-load resistance R_0), was normalized by the R_0 as $\Delta R/R_0$ and plotted.

Supporting Information

Supporting Information is available from the Wiley Online Library or from the author.

Acknowledgements

This work was sponsored by the U.S. Department of Energy, Office of Energy Efficiency and Renewable Energy, Industrial Technologies Program, under contract DE-AC05-00OR22725 with UT-Battelle, LLC.

Conflict of Interest

The authors declare no conflict of interest.

Author Contributions

X.Z. conceived and designed the research; Z.X. carried out the additive manufacturing system setup, performed experiments, measurements, and simulations; H.L. performed the experiments and simulations; S.K. contributed to the experiments; Z.X. and X.Z. wrote the article with contributions from all the authors; X.Z., S.K., and V.K. supervised the project.

Data Availability Statement

The data that support the findings of this study are available from the corresponding author upon reasonable request.

Keywords

carbon fiber composites, digital light processing, self-sensing, tunable stiffness, vat photopolymerization

Received: August 11, 2023
Revised: September 22, 2023
Published online:

- [1] M.-T. Hsieh, C. S. Ha, Z. Xu, S. Kim, H. F. Wu, V. Kunc, X. Zheng, *J. Mater. Res.* **2021**, *36*, 3628.
- [2] Z. Xu, C. S. Ha, R. Kadarn, J. Lindahl, S. Kim, H. F. Wu, V. Kunc, X. Zheng, *Addit. Manuf.* **2020**, *32*, 101106.
- [3] M. Badawi, K. Soudki, *J. Compos. Constr.* **2005**, *9*, 195.
- [4] a) R. Othman, N. I. Ismail, M. Pahmi, M. H. M. Basri, H. Sharudin, A. R. Hemdi, *J. Mech. Manuf.* **2018**, *1*, 144; b) M. Aamir, M. Tolouei-Rad, K. Giasin, A. Nosrati, *Int. J. Adv. Manuf. Technol.* **2019**, *105*, 2289; c) J. J. Andrew, H. Alhashmi, A. Schiffer, S. Kumar, V. S. Deshpande, *Mater. Des.* **2021**, *208*, 109863; d) S. Wang, D. Chung, *Carbon* **2006**, *44*, 2739.
- [5] a) W. Ye, H. Dou, Y. Cheng, D. Zhang, S. Lin, *Polym. Compos.* **2022**, *43*, 7428; b) W. Ye, H. Dou, Y. Cheng, D. Zhang, *Mater. Lett.* **2022**, *317*, 132077.
- [6] A. Y. Chen, S. Baehr, A. Turner, Z. Zhang, G. X. Gu, *Int. J. Lightweight Mater. Manuf.* **2021**, *4*, 468.
- [7] T. Suzuki, J. Takahashi, presented at *Proc. 9th Japan Int. SAMPE Symp., Japan 2005*, https://scholar.google.com/scholar?hl=en&as_sdt=0%2C5&q=Prediction+of+energy+intensity+of+carbon+fiber+reinforced+plastics+for+mass-produced+passenger+cars&btnG=.
- [8] M. B. A. Tamez, I. Taha, *Addit. Manuf.* **2021**, *37*, 101748.
- [9] a) N. J. Gerard, M. Oudich, Z. Xu, D. Yao, H. Cui, C. J. Naify, A. Ikei, C. A. Rohde, X. R. Zheng, Y. Jing, *Phys. Rev. Appl.* **2021**, *16*, 024015; b) M. Oudich, E. Huang, H. Heo, Z. Xu, H. Cui, N. J. Gerard, X. R. Zheng, Y. Jing, *Appl. Phys. Lett.* **2023**, *122*, 171701; c) R. Hensleigh, H. Cui, Z. Xu, J. Massman, D. Yao, J. Berrigan, X. Zheng, *Nat. Electron.* **2020**, *3*, 216; d) C. Wang, W. Ping, Q. Bai, H. Cui, R. Hensleigh, R. Wang, A. H. Brozena, Z. Xu, J. Dai, Y. Pei, *Science* **2020**, *368*, 521; e) H. Cui, D. Yao, R. Hensleigh, H. Lu, A. Calderon, Z. Xu, S. Davaria, Z. Wang, P. Mercier, P. Tarazaga, *Science* **2022**, *376*, 1287; f) A. Cortés, A. Cosola, M. Sangermano, M. Campo, S. González Prolongo, C. F. Pirri, A. Jiménez-Suárez, A. Chiappone, *Adv. Funct. Mater.* **2021**, *31*, 2106774; g) P. Mainik, L. Y. Hsu, C. W. Zimmer, D. Fauser, H. Steeb, E. Blasco, *Adv. Mater. Technol.* **2023**, *2*, 2300727.
- [10] a) Z. Xu, R. Hensleigh, N. J. Gerard, H. Cui, M. Oudich, W. Chen, Y. Jing, X. R. Zheng, *Addit. Manuf.* **2021**, *47*, 102321; b) D. Behera, S. Chizari, L. A. Shaw, M. Porter, R. Hensleigh, Z. Xu, N. K. Roy, L. G. Connolly, X. R. Zheng, S. Saha, *Precis. Eng.* **2021**, *68*, 301; c) D. Behera, S. Chizari, L. A. Shaw, M. Porter, R. Hensleigh, Z. Xu, X. Zheng, L. G. Connolly, N. K. Roy, R. M. Panas, *Precis. Eng.* **2021**, *68*, 197.
- [11] a) A. Badev, Y. Aboualiatim, T. Chartier, L. Lecamp, P. Lebaudy, C. Chaput, C. Delage, *J. Photochem. Photobiol., A* **2011**, *222*, 117; b) T. Schlotthauer, D. Nolan, P. Middendorf, *Addit. Manuf.* **2021**, *42*, 102005.
- [12] a) R. Lakes, *Viscoelastic Materials*, Cambridge University Press, Cambridge **2009**; b) C. P. Chen, R. S. Lakes, *J. Mater. Sci.* **1993**, *28*, 4299.
- [13] a) L. Salari-Sharif, T. A. Schaundler, L. Valdevit, *J. Mater. Res.* **2014**, *29*, 1755; b) L. Salari-Sharif, T. A. Schaundler, L. Valdevit, *J. Eng. Mater. Technol.* **2018**, *140*, 031003; c) M. F. Ashby, *Materials Selection in Mechanical Design*, Butterworth Heinemann, Oxford **1999**; d) H. R. Shercliff, M. F. Ashby, *Encycl. Mater. Sci. Technol.* **2001**, 2429.
- [14] a) B. S. Cook, A. Shamim, M. Tentzeris, *IET Microwaves Antennas Propag.* **2012**, *6*, 1536; b) G. L. Goh, V. Dikshit, R. Koneru, Z. K. Peh, W. Lu, G. D. Goh, W. Y. Yeong, *Int. J. Adv. Manuf. Technol.* **2022**, *120*, 2573; c) C. D. Armstrong, L. Yue, F. Demoly, K. Zhou, H. J. Qi, *Adv. Intell. Syst.* **2023**, *5*, 2200226.